Vladislav L. Sidorov[1,2], Rose K. Baimuratova[1*] ⓘ, Denis V. Korchagin[1] ⓘ, Andrey V. Ivanov[1],
Kamila A. Kydralieva[3] ⓘ, Gulzhian Dzhardimalieva[1,3] ⓘ

*[1]Federal Research Center of Problems of Chemical Physics and Medicinal Chemistry, Russian Academy of Sciences;
Chernogolovka, Moscow region, Russia;*
*[2]Lomonosov Moscow State University, Moscow, Russia;*
*[3]Moscow Aviation Institute (National Research University), Moscow, Russia*
*(\*Corresponding author′s e-mail: Roz_Baz@mail.ru)*

# Magnetically Separable Fe₃O₄/γ-Fe₂O₃@MIL-88b(Fe) and Fe₃O₄/γ-Fe₂O₃@NH₂-MIL-88b(Fe) Composites for the Photocatalytic Degradation of Congo Red Dye

Industry-wide applications of synthetic dyes produce large amounts of dye wastewater that requires treatment. Advanced oxidation processes are considered promising, since they incorporate highly reactive hydroxyl radicals capable of oxidizing most organic pollutants, including most commonly used azo dyes, into carbon dioxide and water. In this regard, iron-based metal-organic frameworks are effective heterogeneous photocatalysts for the generation hydroxyl radicals via Fenton reaction. In this study, Fe3O4/Fe2O3@MIL-88b(Fe) and Fe3O4/γ-Fe2O3@NH2-MIL-88b(Fe) composites were obtained, where Fe3O4/γ-Fe2O3 particles enabled magnetic separation, and Fe-metal-organic frameworks (MOF) coating exhibited photocatalytic activity. These composites were characterized by elemental analysis, FTIR spectra, XRD patterns, magnetization curves, TGA profiles, nitrogen adsorption-desorption isotherms. Using ultraviolet-visible spectroscopy and Congo Red anionic azo dye (CR) as organic pollutant, composites' adsorption kinetics were observed and their photocatalytic activities were studied. As a result, Fe3O4/γ-Fe2O3@MIL-88b(Fe) and Fe3O4/γ-Fe2O3@NH2-MIL-88b(Fe) were both capable photocatalysts for generating hydroxyl radicals from hydrogen peroxide ($H_2O_2$) through Fenton-like reaction with removal efficiencies of CR dye approaching 89 % and 95 %, respectively. Moreover, a higher photocatalytic activity was observed for Fe3O4/γ-Fe2O3@NH2-MIL-88b(Fe), supposedly, due to -NH2 group increasing the electron density on the aryl ring, which stabilized hole localization at the organic linker, increased photoexcited state lifetime and promoted electron transfer onto metal center in Fe3-μ3-O cluster.

*Keywords:* Heterogeneous Fenton-like catalysts, MIL-88b(Fe), NH2-MIL-88b(Fe), Iron-based MOFs, Photocatalysis, magnetic composites, adsorption kinetics, organic pollutants degradation.

## Introduction

Synthetic dyes are extensively utilized in textile, printing, pharmaceutical, cosmetic, food and beverage industries [1–3]. In particular, azo dyes remain as the most commonly implemented dyes due to their superior stability upon being subjected to light irradiation, acidic and basic solutions, oxidation [4]. Estimates suggest that staggering 280,000 tons of untreated dye wastewater are annually discharged into the environment [5].

Organic pollutant removal can be achieved in a number of ways including physical adsorption [6], biological treatment [7] and advanced oxidation processes (AOPs) which incorporate highly reactive hydroxyl radicals (·OH) [8]. While physical adsorption is an inherently simple process, utilized adsorbent gradually turns into solid waste and subsequently requires laborious regeneration [9]. Biological treatment methods are scalable, yet they tend to lose their efficiency when employed for azo dyes degradation [10]. Finally, AOPs are considered promising, since hydroxyl radicals are capable of oxidizing most organic pollutants, including azo dyes, into carbon dioxide ($CO_2$) and water ($H_2O$) [11].

Generally speaking, methods for hydroxyl radicals' generation in wastewater include ozonation, ultrasonication, ultraviolet (UV) irradiation, incorporation of oxidizing agents such as hydrogen peroxide ($H_2O_2$) and various combinations of these processes [12]. Ozonation is mainly encumbered by ozone's limited solubility in water, therefore propagating increased energy and time requirements for treatment[13]. Furthermore, ultrasonication process also specifies high energy consumption [12]. In case of a standalone UV irradiation

organic pollutants tend to partially decompose, leaving harmful intermediates present in water [12]. In this regard, numerous catalysts are being considered to enhance decomposition process, including silver nanoparticles (Ag NPs) [14], various semiconductors [15], such as titanium dioxide (TiO$_2$), zinc oxide (ZnO), gallium arsenide (GaAs), tungsten trioxide (VI) (WO$_3$), gallium phosphide (GaP), cadmium sulfide (CdS) [7]), systems with presence of divalent ferrous ions (Fe$^{2+}$) [12] for a Fenton reaction [16]. Though Ag NPs demonstrate high catalytic activity, they need to be initially activated via complex procedure [15]. Semiconductor materials often possess a large band gap similar to TiO$_2$ (3.2 eV) which prevents them from fully absorbing solar spectrum energy. Additionally, rapid recombination of photogenerated electron/hole pairs in these materials further diminishes quantum efficiency [17]. While Fenton reaction is feasible in the absence of light and demonstrates remarkable efficiency at generating hydroxyl radicals, it traditionally necessitates highly acidic pH (2-3) and implements homogeneous ferrous catalyst, that requires subsequent laborious extraction [12]. Nevertheless, Fenton reaction process can be improved upon by introducing external ultraviolet-visible (UV-Vis) irradiation [18] and simultaneously utilizing heterogeneous ferrous photocatalyst. Moreover, a priority is set on the development of new heterogeneous ferrous photocatalyst materials that initiate Fenton reaction at slightly acidic or neutral pH.

Metal-organic frameworks (MOFs) are porous two- or three-dimensional coordination polymers constructed via self-assembly of inorganic nodes (metal ions or clusters) and organic linkers (bridging ligands) [19]. Owing to the huge number of currently available inorganic nodes and organic linkers MOFs demonstrate an astonishing structure variety, adjustable pore volume and high specific surface area, all of which encourages their use for gas separation and detection, drug delivery, hydrogen storage, adsorption and catalysis [20–22].

Implementation of inorganic nodes with d-block transition metals produces Ti-MOFs, Zr-MOFs [23], Fe-MOFs [20, 24] and Cu-MOFs [25] that possess an optimal bandgap for solar spectrum absorption and can be potentially utilized as UV-Vis photocatalysts for degradation of organic pollutants [18]. It is believed that organic linkers promote charge separation and electron transfer onto metal centers, while also enhancing electron-hole pair transport towards MOF's surface for better performance in redox reactions [20]. Additionally, weak coordination between d-block transition metals and non-bridging ligands propagates the formation of coordination vacancies, resulting in metal centers behavior similar to Lewis acid catalytic sites [18]. Lastly, organic linkers possessing dissimilar double bond conjugation architecture may be used to further improve MOF's photocatalytic properties and its ability for absorbing solar spectrum [18, 20].

One of the most commonly used inorganic nodes in Fe-MOFs (such as MIL-88b(Fe), MIL-101(Fe) and MIL-100(Fe)) is a trinuclear oxo-centered iron (Fe$_3$-μ$_3$-O) cluster [26, 27] with octahedral metal centers. In presence of a visible light irradiation Fe$_3$-μ$_3$-O cluster undergoes excitation and a subsequent electron transfer from O$^{2-}$ to Fe$^{3+}$, forcing metal center reduction [20], while Fe-MOF's porous structure ensures sufficient diffusion of reagents towards reduced metal centers. Evidently, nonbridging ligands in metal center's coordination sphere are easily substituted for Lewis bases. In this regard, MIL-88b(Fe), being a highly flexible Fe-MOF with 1,4-benzenedicarboxylates (BDC) as organic linkers bridging together Fe$_3$-μ$_3$-O clusters, possesses high photocatalytic activity and is therefore considered as a promising heterogeneous Fenton catalyst [24, 28, 29]. As a Lewis base, H$_2$O$_2$ easily adsorbs onto Fe$_3$-μ$_3$-O clusters, while electron-rich benzenedicarboxylate (BDC) linkers promote photoinduced reduction of Fe$^{3+}$ into Fe$^{2+}$, which initiates Fenton reaction. Despite MIL-88b(Fe)'s flexibility in presence of polar solvents such as water (H$_2$O), its topology remains the same, yet its pore volume alters, potentially further enhancing reagents' diffusion towards metal centers. In contrast to homogenous Fe$^{2+}$/Fe$^{3+}$ catalyst, heterogeneous MIL-88b(Fe) is capable of initiating Fenton reaction at less acidic pH (4-6) [28]. It is worth noting that at pH from 4 to 5 a miniscule amount of ferrous ions is released into solution; however they do not exhibit noticeable catalytic activity, since homogeneous Fenton requires higher acidity [28]. At basic pH (10) MIL-88b(Fe)'s adsorption capacity and photocatalytic activity diminish quickly, which may be linked to compromised integrity of the porous structure [28, 29]. Otherwise, MIL-88b(Fe) retains its performance over a wide range of pH (4-8) [28].

MOF's adsorption and photocatalytic performance can be enhanced by implementing organic linkers with additional functional groups [30]. Namely, insertion of 2-amino-1,4-benzenedicarboxylate (NH$_2$-BDC) linkers between Fe$_3$-μ$_3$-O clusters produces NH$_2$-MIL-88b(Fe) that inherits MIL-88b(Fe)'s original structure. Amino groups enable additional mechanisms for sorbate-sorbent interaction, including emergence of covalent bonds with an electron-deficient sorbate [30], hydrogen bonds [31], electrostatic and ionic interactions [32], chelation [33]. When determining optimal pH one should also consider potential electrostatic and ionic repulsion between protonated amino group and different ionic forms of sorbate molecules [32, 34, 35].

Another important aspect of MOF is its ability to retain adsorption and photocatalytic performance over repeated use cycles. In this regard, both MIL-88b(Fe) [26] and NH$_2$-MIL-88b(Fe) [35] exhibit good long-term stability with little decrease in photocatalytic activity after several successive cycles of organic pollutants decomposition. Significant loss of photocatalytic activity only occurs at prolonged irradiation intervals (more than 400 hours), when almost all organic linkers undergo decarboxylation [36].

To improve MOF's practical reusability, it can be applied as a coating on the magnetic particle's surface, enabling magnetic separation of MOF from aqueous medium. Compared with conventional filtration and centrifugation processes, removal of heterogeneous catalysts via magnetic separation is considered promising since it reduces solvents and auxiliaries use, as well as financial and time expenses [37]. Magnetite (Fe$_3$O$_4$) and maghemite ($\gamma$-Fe$_2$O$_3$) particles are generally chosen as magnetic carriers due to their environmental friendliness, straightforward synthesis and sufficient saturation magnetization values. Standalone iron oxide particles also catalyze the decomposition of organic pollutants [38, 39], yet they possess high surface energy, which often causes their aggregation, leading to an overall decrease in catalytic activity [40]. Nevertheless, Fe$_3$O$_4$ particles coated with MIL-100(Fe) photocatalyst result in a Fe$_3$O$_4$@MIL-100(Fe) composite, which decomposes methylene blue more efficiently than TiO$_2$ and is easily removed from solution with a strong magnet [41].

While numerous evidences prove MIL-88b(Fe)'s and NH$_2$-MIL-88b(Fe)'s acceptable adsorption and photocatalytic performance, few studies implement magnetic separation of Fe-MOFs from aqueous medium and examine their ability to decompose azo dyes. Therefore, this study primarily focuses on the synthesis of Fe$_3$O$_4$/$\gamma$-Fe$_2$O$_3$@MIL-88b(Fe) and Fe$_3$O$_4$/$\gamma$-Fe$_2$O$_3$@NH$_2$-MIL-88b(Fe) composites, where Fe$_3$O$_4$/$\gamma$-Fe$_2$O$_3$ particles enable magnetic separation, and Fe-MOF coating exhibits photocatalytic activity [40]. Fe-MOFs were constructed through rational approach of utilizing pre-synthesized Fe$_3$-$\mu_3$-O acetate clusters as secondary building units [42–45]. Essentially, Fe$_3$-$\mu_3$-O clusters' geometry strictly determined the coordination of organic linkers, which produced isoreticular Fe-MOFs with desired topology. Finally, Fe$_3$O$_4$/$\gamma$-Fe$_2$O$_3$@MIL-88b(Fe) and Fe$_3$O$_4$/$\gamma$-Fe$_2$O$_3$@NH$_2$-MIL-88b(Fe) were both capable photocatalysts for generating hydroxyl radicals from H$_2$O$_2$ through Fenton-like reaction with removal efficiencies of Congo Red dye approaching 89 % and 95 %, respectively.
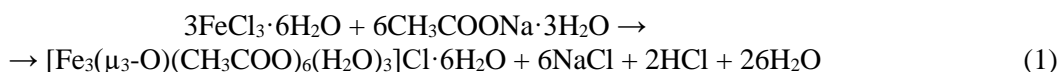
*Experimental*

*Starting Materials*

Ferric chloride hexahydrate (FeCl$_3$·6H$_2$O, puriss.), ferrous chloride tetrahydrate (FeCl$_2$·4H$_2$O, puriss.), sodium acetate trihydrate (CH$_3$COONa·3H$_2$O, puriss.), ethanol (C$_2$H$_5$OH, 96,5 %, pur.), aqueous ammonia (NH$_4$OH, 25 %, pur.), hydrogen peroxide (H$_2$O$_2$, 30 %, pur.), glacial acetic acid (CH$_3$COOH, 99,8 %, puriss.), potassium hydroxide (KOH, puriss.) were supplied by Ruskhim chemical company, while 1,4-benzenedicarboxylic (terephthalic) acid (BDCa, C$_8$H$_6$O$_4$, 98 %) and 2-amino-1,4-benzenedicarboxylic (2-aminoterephthalic) acid (NH$_2$-BDCa, C$_8$H$_7$NO$_4$, 99 %) were purchased from Sigma-Aldrich.

*Preparation of Oxo-Centered Iron Acetate Cluster*

To synthesize oxo-centered iron acetate ([Fe$_3$($\mu_3$-O)(CH$_3$COO)$_6$(H$_2$O)$_3$]Cl·6H$_2$O) cluster, preheated (50 °C) aqueous solutions of 3M FeCl$_3$·6H$_2$O (127.22 g, 150 mL) and 6M CH$_3$COONa·3H$_2$O (122.42 g, 150 mL) were poured in 600 mL beaker and magnetically stirred (500 rpm) at 50 °C for 30 minutes [45]:

$$3FeCl_3 \cdot 6H_2O + 6CH_3COONa \cdot 3H_2O \rightarrow$$
$$\rightarrow [Fe_3(\mu_3\text{-}O)(CH_3COO)_6(H_2O)_3]Cl \cdot 6H_2O + 6NaCl + 2HCl + 26H_2O \qquad (1)$$

The reaction mixture was then poured in 150 mm × 75 mm crystallizing dish and left to cool down overnight. In the following days water was allowed to slowly evaporate. The resulting precipitate was filtered in a Buchner funnel and washed with cold ethanol (–18 °C). After that, the precipitate was dried in a vacuum (10$^{-3}$ Torr, 40 °C, 10 h). Yield: 88.77 g (80 %). Found (wt. %): C, 19.7±0.13; H, 5.2±0.05; Fe, 22.9±0.5. Calculated for ([Fe$_3$($\mu_3$-O)(CH$_3$COO)$_6$(H$_2$O)$_3$]Cl·6H$_2$O) (wt. %): C, 19.60; H, 4.93; Fe, 22.78; Cl, 4.82. FTIR (KBr, vmax/cm-1): 3523 $\nu$(O-H); 2929 $\nu$(C-H); 1601 vas(COO-), 1520 vas(COO-), 1444 vs(COO-); 665 $\nu$(Fe-O).

*Preparation of Fe$_3$O$_4$/$\gamma$-Fe$_2$O$_3$@Fe-MOF Composites*

To obtain each Fe$_3$O$_4$/$\gamma$-Fe$_2$O$_3$@Fe-MOF composite a two-stage process was implemented. At the first stage, Fe$_3$O$_4$/$\gamma$-Fe$_2$O$_3$ particles were synthesized through Elmore's approach [46]. Namely, in presence of argon atmosphere 10.1 g of FeCl$_3$·6H$_2$O, 3.71 g of FeCl$_2$·4H$_2$O and 250 mL of deionized water were added into 500 mL three neck round bottom flask and vigorously mixed with mechanical stirrer (2000 rpm) until

complete dissolution. While maintaining mechanical stirrer speed and argon flow to the flask, 22.5 mL of NH₄OH (25 %) were added drop-wise to cause precipitation:

$$2FeCl_3 + FeCl_2 + 8NH_4OH \rightarrow Fe_3O_4\downarrow + 8NH_4Cl + 4\,H_2O \qquad (2)$$

Despite argon atmosphere inside the flask, Fe₃O₄ still underwent partial oxidation into γ-Fe₂O₃, thus producing Fe₃O₄/γ-Fe₂O₃ particles. At the second stage, Fe₃O₄/γ-Fe₂O₃ particles were coated with Fe-MOF through rational approach of utilizing pre-synthesized [Fe₃(μ₃-O)(CH₃COO)₆(H₂O)₃]Cl·6H₂O clusters as secondary building units [42]. To obtain Fe₃O₄/γ-Fe₂O₃@MIL-88b(Fe) composite, 8.48 g of BDCa were added to reaction mixture in the flask while stirring speed further remained the same. After the dissolution of BDCa, 12.4 g of [Fe₃(μ₃-O)(CH₃COO)₆(H₂O)₃]Cl·6H₂O were finally added for an exchange reaction to occur, which resulted in nonbridging acetate ligands being substituted with BDCa linkers, thus producing desired MIL-88b(Fe) coating (Scheme). To obtain Fe₃O₄/γ-Fe₂O₃@NH₂-MIL-88b(Fe) composite same steps were carried out with 9.10 g of NH₂-BDCa. Finally, each composite precipitate was filtered in a Buchner funnel and washed with warm (65 °C) deionized water. After that, precipitates were dried in a vacuum (10⁻³ Torr, 50 °C, 5 h). Yield: 17.06 g (98 %) and 12.35 g (72 %) for Fe₃O₄/γ-Fe₂O₃@MIL-88b(Fe) and Fe₃O₄/γ-Fe₂O₃@NH₂-MIL-88b(Fe), respectively.
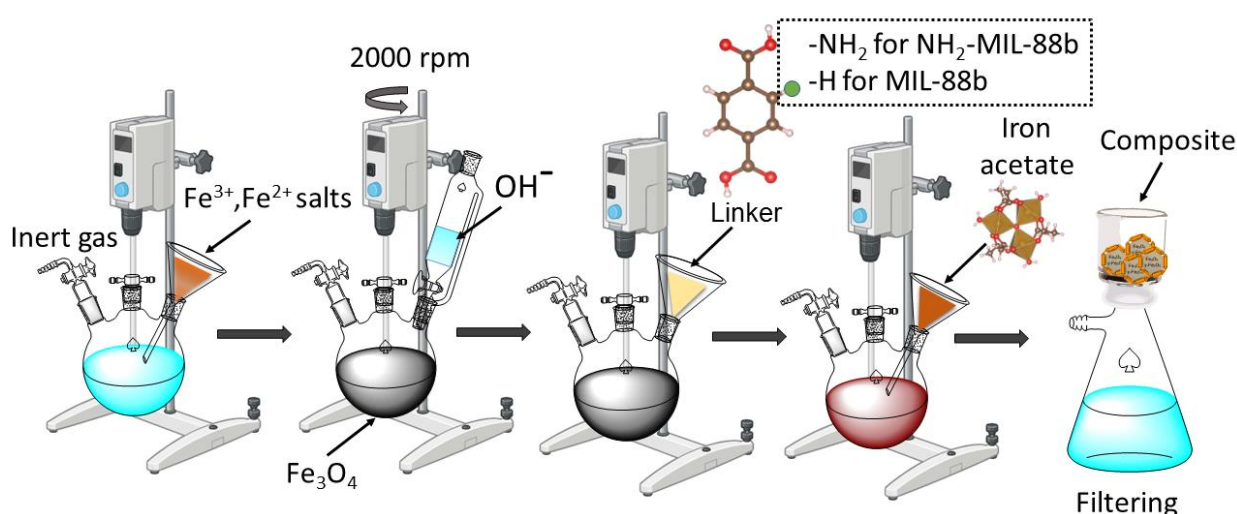


Scheme. Schematic representation of the Fe₃O₄/γ-Fe₂O₃@MOF composites' synthesis process

*General Methods*

C, H, N contents were determined through combustion analysis (Elementar vario MICRO cube, Germany), while Fe content was measured using atomic absorption spectroscopy (AAS) (Carl Zeiss AAS-3, Germany). Oxygen content was subsequently calculated via the equation: O (wt. %) = 100 − (C + H + N + Fe). Fourier-transform infrared (FTIR) spectra of the composites were recorded in the range of 4000–500 cm⁻¹ (PerkinElmer Spectrum 100, USA) using attenuated total reflection (ATR) technique. To further evaluate composites' structure and quantify Fe₃O₄ and γ-Fe₂O₃ phases, powder X-ray diffraction (XRD) analysis was conducted under Cu-Kα radiation (λ = 1.5406 Å) (Aeris Benchtop, Malvern PANalytical, the Netherlands). The magnetization curves of the composites were recorded at room temperature (25 °C) with field ranging from –10 kOe to 10 kOe on a vibrating sample magnetometer (VSM) (CFMS, Cryogenic Ltd, Japan). To study composites' thermal stability thermogravimetric analysis (TGA) was conducted (Mettler Toledo TGA/SDTA851e, Switzerland) from 25 to 550 °C at a heating rate of 10 °C/min in nitrogen atmosphere. Nitrogen adsorption-desorption isotherms were obtained at -196 °C (Quantachrome Autosorb-1, USA) and subsequently used to determine Brunauer–Emmett–Teller (BET) surface area and average pore diameter of each composite. Sample pretreatment was performed at the absorber degassing station by purging the sample with helium and then evacuating to 10⁻⁵ Torr at 423 K.

*Adsorption Studies*

Prior to exploring photocatalytic activity of composites, their adsorption capacity was carefully examined. Namely, adsorption experiments implemented Congo Red anionic azo dye (CR) (Fig. S1*a*) as an organic pollutant which had to be removed from aqueous solution. While CR can exist both in protonated (below

the pH of 3.0, blue-colored solution) and unprotonated (above the pH of 5.2, red-colored solution) forms, the latter one exhibits ultraviolet-visible (UV-Vis) spectrum with a distinct -N=N- group peak at 498 nm. Therefore, a height of this peak was used to specifically monitor CR concentration in a solution with accordingly adjusted pH (above 6.0) via UV-V is spectrophotometer (Speks SSP-705, Spektroskopicheskie sistemy, Russian Federation). Before measuring UV-Vis spectra, each CR solution sample/aliquot was centrifuged at 11000 rpm for 4 minutes to isolate it from the composite particles. In case of kinetic observations magnetic separation of composites via strong neodymium magnet was preliminarily implemented. Finally, CR removal efficiency Re (%) and adsorption capacity q (mg/g) were denoted as follows:

$$Re = \frac{(C_0 - C)}{C_0} \times 100\%,$$

$$q = \frac{(C_0 - C)V}{m},$$

where $C_0$ (mg/L) is the initial CR concentration; $C$ (mg/L) is CR concentration at a given time; $V$ (L) is solution's volume and m ($g$) is composite's mass.

*Effect of Composite Dosage*

In a typical experiment, 10 mL of CR solution (60 mg/L, 25 °C), a specific dosage of selected composite (5, 10, 15, 20, 25, 30 mg) and a drop of 1M KOH solution (approx. 0.1 mL) were added into 50 mL conical flask, which was then placed on a reciprocating laboratory shaker PE-6500 (ECROSKHIM) for 45 minutes, after which samples of CR solution were taken. Throughout these experiments an optimal concentration of composite for subsequent studies was determined.

*Effect of pH*

Each experiment was started with 50 mL of CR solution (60 mg/L, 25 °C) and 100 mg of selected composite (2 g/L) being added to a 100 mL conical flask. Immediately after that, the conical flask was placed on the reciprocating laboratory shaker PE-6500 (ECROSKHIM) for 45 minutes, while CR solution's pH was adjusted and maintained accordingly by a drop-wise addition of 0.1M KOH solution. For pH readout a digital pH-meter pH-410 (AKVILON) with a combination pH electrode (Ag/AgCl reference system) was implemented. After 45 minutes had passed, samples of CR solution were taken. Ultimately, each composite's maximum adsorption capacity was evaluated.

*Adsorption Kinetics*

To observe adsorption kinetics a following adsorption experiment was conducted for each composite. Firstly, 50 mL of CR solution (60 mg/L, 25 °C) were poured into 150 mL (75×45 mm) crystallizing dish and a stir bar (ferrite rod in a glass ampule) was added. Magnetic stirrer MSH 300 (BioSan) was turned on and its speed was set at approximately 500 rpm. After that, 0.04 mL of glacial acetic acid was added into CR solution. According to the digital pH-meter pH-410 (AKVILON) with the combination pH electrode (Ag/AgCl reference system) a pH value of 3.5 was reached. In fact, this exact pH was subsequently used in photocatalytic degradation experiments, since it provided an optimal $Fe^{2+}/Fe^{3+}$ ratio for Fenton reaction [47]. Lastly, 100 mg of selected composite (2 g/L) were added to CR solution, which marked experiment's starting point. Throughout the experiment, which lasted for 150 minutes, the crystallizing dish was covered with a hood that blocked off any incident light, thus excluding photocatalytic degradation as a contributing factor towards CR removal efficiency. Every 15 minutes, composite was mostly gathered at crystallizing dish's bottom via strong neodymium magnet and 2.5 mL aliquot was taken from CR solution. To separate the remaining small composite particles, this aliquot was centrifuged, and 2.0 mL of supernatant CR solution were carefully transferred into a separate test tube. After that, precisely 1 drop of 1M KOH solution was added to raise the pH above 6.0 and convert CR back into its unprotonated form for subsequent UV-Vis spectra measurement.

*Photocatalytic Activity Study*

The experiment to study the photocatalytic activity of each composite started with the same procedure used for observing adsorption kinetics. Namely, 50 mL of CR solution (60 mg/L, 25°C), 0.04 mL of glacial acetic acid and the stir bar were added into 150 mL (75×45 mm) crystallizing dish. The magnetic stirrer's speed was set at approximately 500 rpm and remained the same throughout whole experiment. The experiment's starting point was marked when 100 mg of selected composite (2 g/L) were added to the solution. In the first 45 minutes of the experiment the crystallizing dish was covered with a hood that blocked off any incident light. After 45 minutes had passed, the hood was removed and 1 mL of $H_2O_2$ 30 % (176 mM) was added to the solution. At the same time a 26W UV lamp (Camelion, 365 nm) was turned on and placed di-

rectly above the solution's surface at a distance of 1–2 cm. The experiment lasted a total time of 150 minutes, during which every 15 minutes 2.5 mL aliquots of CR solution were taken and treated identically to ones in observing adsorption kinetics. Finally, a control experiment was conducted using the same procedure but without the composite.

## Results and Discussion

### Characterization of $Fe_3O_4/\gamma$-$Fe_2O_3$@Fe-MOF Composites

#### Design Approach

Currently, there are four main techniques of obtaining composites which combine MOFs with magnetic particles (MPs): mixing pre-synthesized MPs with MOF, embedding MPs into MOF's pores, encapsulation of MP with an interface material that promotes MOF application, layer-by-layer growth of MOF coating directly on MP's surface [48]. In this study, the latter technique was implemented to obtain $Fe_3O_4/\gamma$-$Fe_2O_3$@MIL-88b(Fe) and $Fe_3O_4/\gamma$-$Fe_2O_3$@$NH_2$-MIL-88b(Fe) composites, where $Fe_3O_4/\gamma$-$Fe_2O_3$ particles enable magnetic separation, and Fe-MOF coating exhibits photocatalytic activity. Since BDCa and $NH_2$-BDCa were added before $[Fe_3(\mu_3$-$O)(CH_3COO)_6(H_2O)_3]Cl\cdot6H_2O$ cluster, they effectively functionalized $Fe_3O_4/\gamma$-$Fe_2O_3$ particles' surface, enabling subsequent layer-by-layer growth of MOF coating [48].

Usually, a standard technique for MOF creation utilizes metal salts to generate inorganic nodes during MOF's self-assembly process. However, if MOF incorporates $Fe_3$-$\mu_3$-O or similar clusters as inorganic nodes, they may not be generated sufficiently, thus altering MOF's structure [49] and producing polycrystalline and amorphous structures [50]. Therefore, in this study Fe-MOFs were constructed by a rational approach of using pre-synthesized $Fe_3$-$\mu_3$-O acetate clusters as secondary building units [42–45]. Moreover, $Fe_3$-$\mu_3$-O clusters' geometry strictly determined the coordination of BDC or $NH_2$-BDC linkers, which produced isoreticular Fe-MOFs with desired topology [51, 52].

#### Elemental analysis

The total composition of the synthesized composites was determined by elemental analysis (Table 1).

T a b l e   1

**C, H, N, Fe, O contents (wt. %) of Fe-MOFs and synthesized composites**

| Sample | C | H | N | Fe | O |
|---|---|---|---|---|---|
| MIL-88b(Fe)[53] | 36.4 | 5.6 | – | 21.3 | 36.6 |
| MIL-88b(Fe)[42] | 38.5 | 2.6 | – | 22.3 | 36.6 |
| $NH_2$-MIL-88b(Fe)[42] | 36.6 | 3.0 | 4.6 | 22.3 | 33.5 |
| $Fe_3O_4/\gamma$-$Fe_2O_3$@MIL-88b(Fe) | 21.1 | 3.0 | – | 33.9 | 41.4 |
| $Fe_3O_4/\gamma$-$Fe_2O_3$@$NH_2$-MIL-88b(Fe) | 14.1 | 2.4 | 1.3 | 39.6 | 42.6 |

In contrast with isolated MIL-88b(Fe) [53] and $NH_2$-MIL-88b(Fe) [42], carbon content has decreased to 14.1–21.1 wt. % and iron content has increased to 33.9–39.6 wt. %, which confirms the presence of both $Fe_3O_4/\gamma$-$Fe_2O_3$ particles and Fe-MOFs in composites' structure. According to carbon content data, the mass fraction of Fe-MOF coating amounted to 57.8±1.5 % in $Fe_3O_4/\gamma$-$Fe_2O_3$@MIL-88b(Fe) composite, which was approximately 20 % more than in the $Fe_3O_4/\gamma$-$Fe_2O_3$@$NH_2$-MIL-88b(Fe) (38.5±1.5 %).

#### FTIR Spectra

To further confirm composites' structure, FTIR spectra of $Fe_3O_4/\gamma$-$Fe_2O_3$@MIL-88b(Fe) (Fig. 1a) and $Fe_3O_4/\gamma$-$Fe_2O_3$@$NH_2$-MIL-88b(Fe) (Fig. 1b) were compared with ones of $Fe_3O_4$, Fe-MOFs and organic linkers. The bands at 1542–1561 cm-1 and 1376–1407 cm-1 corresponded to asymmetric and symmetric stretching vibrations of Fe-bound carboxylate groups in Fe-MOFs, respectively. Additionally, C-H stretching and bending vibrations in aromatic rings of organic linkers were represented by the bands at 2928–2933 cm-1 and 728–768 $cm^{-1}$, respectively. The band at 555–564 $cm^{-1}$ was ascribed to Fe-O stretching vibrations both in $Fe_3O_4$ and Fe-MOFs. For $NH_2$-MIL-88b(Fe) (Figure 1b) symmetric and asymmetric stretching vibrations of the -$NH_2$ group were represented by the two bands at 3455 cm-1 and 3373 cm-1, respectively, while the band at 1249 cm-1 was due to C-N stretching vibration [54]. These characteristic bands of $Fe_3O_4$ and Fe-MOFs were also inherent in composites, which ultimately confirmed their structure.
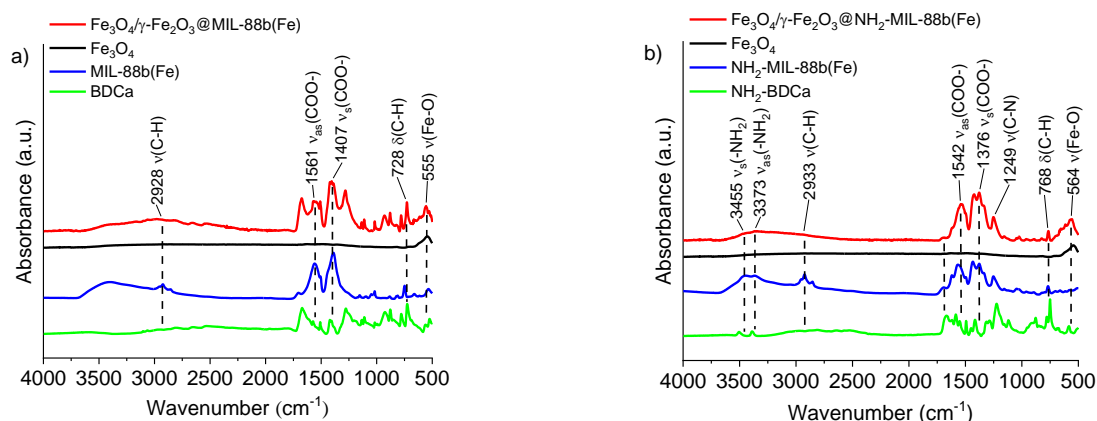
Figure 1. FTIR spectra of Fe$_3$O$_4$/γ-Fe$_2$O$_3$@MIL-88b(Fe) (*a*) and Fe$_3$O$_4$/γ-Fe$_2$O$_3$@NH$_2$-MIL-88b(Fe) (*b*), Fe$_3$O$_4$, Fe-MOFs and organic linkers

*XRD patterns*

Since Fe$_3$O$_4$ underwent partial oxidation into γ-Fe$_2$O$_3$ during composite synthesis, XRD patterns were recorded (Fig. 2) to determine the actual ratio of Fe(II) and Fe(III) (i.e. $x$ = Fe(II)/Fe(III)) in Fe$_3$O$_4$/γ-Fe$_2$O$_3$ particles. Both of Fe$_3$O$_4$ and γ-Fe$_2$O$_3$ are inherently cubic phases with identical (311), (400), (422), (511), (440) reflections and slightly different unit cell length a values [55, 56]. As a consequence, there is a little offset between Fe$_3$O$_4$ and γ-Fe$_2$O$_3$ reflection peaks. In case of Fe$_3$O$_4$/γ-Fe$_2$O$_3$ particles, this offset can be exploited for determining the average a value:

$$a = \frac{\lambda}{2*\sin\left(\frac{2\theta}{2}\right)}\sqrt{\left(h^2 + k^2 + l^2\right)}, \tag{5}$$

where λ is radiation source wavelength; h, k, l are Miller indices. Using known values of $x$ = 0.5, $a$ = 8.335–8.340 Å for Fe$_3$O$_4$ (ICDD–PDF 19-629) and $x$ = 0, $a$ = 8.396–8.400 Å for γ-Fe$_2$O$_3$ (ICDD–PDF 39-1346), the average a was converted into the actual Fe(II)/Fe(III) ratio in Fe$_3$O$_4$/γ-Fe$_2$O$_3$ particles of Fe$_3$O$_4$/γ-Fe$_2$O$_3$@MIL-88b(Fe) and Fe$_3$O$_4$/γ-Fe$_2$O$_3$@NH$_2$-MIL-88b(Fe) composites (Table 2). Finally, the Fe$_3$O$_4$ content was 22.7 wt. % and 72.2 wt. % for Fe$_3$O$_4$/γ-Fe$_2$O$_3$ particles in Fe$_3$O$_4$/γ-Fe$_2$O$_3$@MIL-88b(Fe) and Fe$_3$O$_4$/γ-Fe$_2$O$_3$@NH$_2$-MIL-88b(Fe), respectively.

Table 2

**Average unit cell length *a* (Å), Fe(II)/Fe(III) *x* ratio and Fe$_3$O$_4$ content (wt. %) for Fe$_3$O$_4$/γ-Fe$_2$O$_3$ particles in the composites**

| Sample | *a* | *x* | Fe$_3$O$_4$ |
|---|---|---|---|
| Fe$_3$O$_4$/γ-Fe$_2$O$_3$@MIL-88b(Fe) | 8.346 | 0.094 | 22.7 |
| Fe$_3$O$_4$/γ-Fe$_2$O$_3$@NH$_2$-MIL-88b(Fe) | 8.375 | 0.332 | 72.2 |
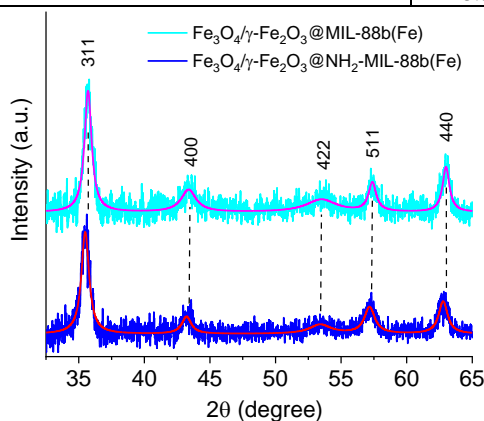


Figure 2. XRD patterns of Fe$_3$O$_4$/γ-Fe$_2$O$_3$@MIL-88b(Fe) and Fe$_3$O$_4$/γ-Fe$_2$O$_3$@NH$_2$-MIL-88b(Fe) composites

It should be noted that reflections intrinsic to MIL-88b(Fe) and NH$_2$-MIL-88b(Fe) (Fig. S2) were not present in the 5–30° range of the recorded XRD patterns. Supposedly, guest-responsive structural flexibility [57–59] induces Fe-MOFs' breathing phenomenon [53, 60, 61], which ultimately alters unit cell volume of Fe-MOFs during solvation and desolvation processes. Therefore, it was proposed that MIL-88b(Fe) and NH$_2$-MIL-88b(Fe) reflections have shifted towards unrecorded small angles. Previously, it was shown for MIL-88b(Fe) that water molecules cause reorientation of Fe$_3$-μ$_3$-O clusters and BDC linkers via rotation about the O-O axis in carboxylate groups [62]. In this regard, MIL-88B(Fe)/Fe$_3$S$_4$ [63] and MIL-88b/nanorods [53] composites exhibit similar behavior.

*Magnetization Curves*

To study the effect of Fe-MOF coating on Fe$_3$O$_4$/γ-Fe$_2$O$_3$ particles' magnetic properties, magnetization curves for Fe$_3$O$_4$/γ-Fe$_2$O$_3$@MIL-88b(Fe) and Fe$_3$O$_4$/γ-Fe$_2$O$_3$@NH$_2$-MIL-88b(Fe) composites were recorded (Fig. 3).
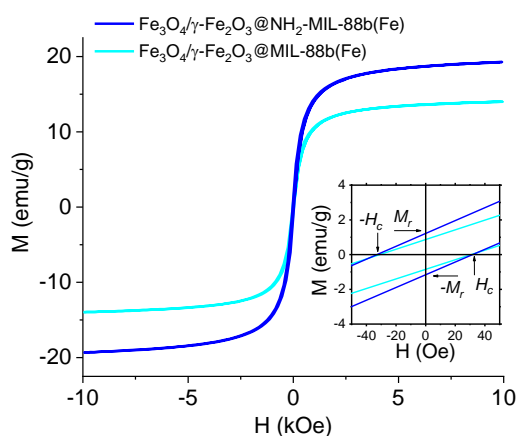


Figure 3. Magnetization curves of Fe$_3$O$_4$/γ-Fe$_2$O$_3$@MIL-88b(Fe)
and Fe$_3$O$_4$/γ-Fe$_2$O$_3$@NH$_2$-MIL-88b(Fe) composites at room temperature (25 °C)

As expected [64–66], magnetic hysteresis was retained for ferromagnetic Fe$_3$O$_4$/γ-Fe$_2$O$_3$ particles in both composites. For quantitative analysis saturation magnetization Ms, remanent magnetization Mr and coercivity Hc were extracted from composite magnetization curves (Table 3). In contrast with isolated Fe$_3$O$_4$ and γ-Fe$_2$O$_3$ particles saturation magnetization has decreased to 14-19 emu/g as a result of non-magnetic Fe-MOF coating being present. Since Ms value of Fe$_3$O$_4$/γ-Fe$_2$O$_3$@MIL-88b(Fe) composite was approximately 25 % smaller than that of Fe$_3$O$_4$/γ-Fe$_2$O$_3$@NH$_2$-MIL-88b(Fe), an inverse correlation between saturation magnetization and Fe-MOF's mass fraction has been established by elemental analysis. Similarly, remanent magnetization values were 0.9 and 1.2 emu/g for Fe$_3$O$_4$/γ-Fe$_2$O$_3$@MIL-88b(Fe) and Fe$_3$O$_4$/γ-Fe$_2$O$_3$@NH$_2$-MIL-88b(Fe), respectively. Both composites exhibited identical reduced coercivity of 33 Oe. Finally, saturation magnetization values were sufficient to perform magnetic separation of composites from aqueous solution using a strong neodymium magnet.

T a b l e  3

**Saturation magnetization *M$_s$* (emu/g), remanent magnetization *M$_r$* (emu/g)
and coercivity *H$_c$* (Oe) of Fe$_3$O$_4$, γ-Fe$_2$O$_3$ and synthesized composites**

| Sample | $M_s$ | $M_r$ | $H_c$ |
|---|---|---|---|
| Fe$_3$O$_4$ [64,65] | 70-80 | 4-7 | 70 |
| γ-Fe$_2$O$_3$ [65,66] | 50-70 | 4-7 | 50 |
| Fe$_3$O$_4$/γ-Fe$_2$O$_3$@MIL-88b(Fe) | 14 | 0.9 | 33 |
| Fe$_3$O$_4$/γ-Fe$_2$O$_3$@NH$_2$-MIL-88b(Fe) | 19 | 1.2 | 33 |

*TGA Profiles*

Thermostability of Fe$_3$O$_4$/Fe$_2$O$_3$@MIL-88b(Fe) and Fe$_3$O$_4$/γ-Fe$_2$O$_3$@NH$_2$-MIL-88b(Fe) was assessed using TGA profiles (Fig. 4a). Both composites exhibited similar TGA profiles with three main weight loss steps. The high-volatility first step (up to 220-230 °C) was due to guest water molecules being released from

Fe-MOF coating. The second step (up to 384-406 °C) was assumed to represent the decarboxylation of -COO- groups in organic linkers [34]. The third step lasted up to 525 °C and was associated with irreversible degradation of Fe-MOFs' structure. To further quantify composite thermostability, TGA derivative (dTGA) profiles were plotted (Fig. 4b) to determine the temperatures of maximum weight loss rates $T_{max1}$, $T_{max2}$ (above 300 °C), $T_{max3}$ (above 440 °C) for each TGA step (Table 4). In contrast to $Fe_3O_4/Fe_2O_3@MIL$-88b(Fe), a slight increase in $T_{max2}$ value was observed for $Fe_3O_4/\gamma$-$Fe_2O_3@NH_2$-MIL-88b(Fe), which may be attributed to $-NH_2$ group engagement in electrostatic and hydrogen bond interactions. In fact, $NH_2$-MIL-88b(Fe) also possessed a higher $T_{max2}$ value than MIL-88b(Fe). After TGA completion a larger final weight was observed for $Fe_3O_4/\gamma$-$Fe_2O_3@NH_2$-MIL-88b(Fe) composite (Table 4), which could be partially related to the smaller mass fraction of Fe-MOF coating.
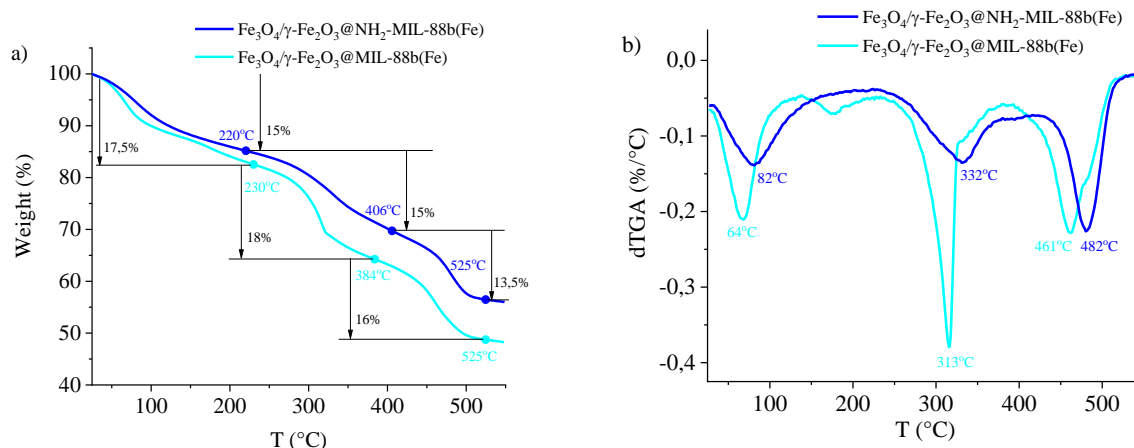


Figure 4. TGA (*a*) and dTGA (*b*) profiles of $Fe_3O_4/\gamma$-$Fe_2O_3@MIL$-88b(Fe)
and $Fe_3O_4/\gamma$-$Fe_2O_3@NH_2$-MIL-88b(Fe) composites at a heating rate of 10 °C/min

Table 4

**Temperatures of maximum weight loss rates $T_{max1}$, $T_{max2}$, $T_{max3}$ (°C) and final weight FW (%) of Fe-MOFs and synthesized composites**

| Sample | $T_{max1}$ | $T_{max2}$ | $T_{max3}$ | *FW* |
|---|---|---|---|---|
| MIL-88b(Fe) [42] | 60 | 328 | 462 | 49 |
| $NH_2$-MIL-88b(Fe) [42] | 61 | 346 | 450 | 56 |
| $Fe_3O_4/\gamma$-$Fe_2O_3@MIL$-88b(Fe) | 64 | 313 | 461 | 48 |
| $Fe_3O_4/\gamma$-$Fe_2O_3@NH_2$-MIL-88b(Fe) | 82 | 332 | 482 | 56 |

*Nitrogen Adsorption-Desorption Isotherms*

To study composite porosity, nitrogen adsorption-desorption isotherms were obtained for $Fe_3O_4/\gamma$-$Fe_2O_3@MIL$-88b(Fe) and $Fe_3O_4/\gamma$-$Fe_2O_3@NH_2$-MIL-88b(Fe) at –196 °C (Fig. 5). Before the measurement of nitrogen adsorption-desorption isotherm, each composite was pretreated at 150 °C for 2 hours. According to IUPAC classification the composites exhibited type IV nitrogen adsorption-desorption isotherms, suggesting Fe-MOF mesoporous structure. The hysteresis loop, specific for capillary condensation in the mesopores, was apparent for both $Fe_3O_4/\gamma$-$Fe_2O_3@MIL$-88b(Fe) and $Fe_3O_4/\gamma$-$Fe_2O_3@NH_2$-MIL-88b(Fe).
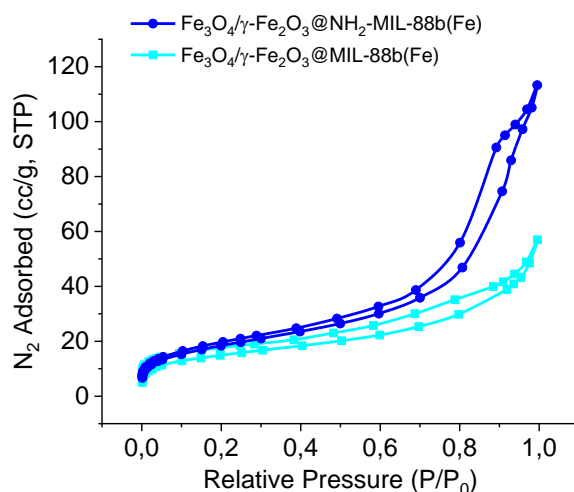
Figure 5. Nitrogen adsorption-desorption isotherms of $Fe_3O_4/\gamma-Fe_2O_3@MIL-88b(Fe)$
and $Fe_3O_4/\gamma-Fe_2O_3@NH_2-MIL-88b(Fe)$ composites at -196 °C

Ultimately, the composite BET surface area $S_{BET}$, as well as Barret-Joyner-Halenda (BJH) pore volume $V$ and average diameter $d$ were determined (Table 5). Additionally, t-plot method was implemented to assess micropore volume $V_{micro}$ and surface area $S_{micro}$ (Table 5). The $S_{BET}$ values of $Fe_3O_4/\gamma-Fe_2O_3@MIL-88b(Fe)$ and $Fe_3O_4/\gamma-Fe_2O_3@NH_2-MIL-88b(Fe)$ were 54 and 68 $m^2/g$, respectively. Depending on synthesis methodology MIL-88b(Fe) and $NH_2-MIL-88b(Fe)$ BET surface can range from 14 to 303 $m^2/g$ [26, 42, 67]. In comparison with isolated Fe-MOFs, reduced $S_{BET}$ values of the composites may be attributed to partial encapsulation of $Fe_3O_4/\gamma-Fe_2O_3$ particles inside Fe-MOFs' pores during synthesis. Nevertheless, $Fe_3O_4/\gamma-Fe_2O_3@NH_2-MIL-88b(Fe)$ expectably possessed slightly increased $S_{BET}$, $V$, $d$ values than those of $Fe_3O_4/\gamma-Fe_2O_3@MIL-88b(Fe)$ [68].

T a b l e  5

**BET surface area $S_{BET}$ ($m^2/g$), BJH pore volume $V$ ($cm^3/g$) and diameter $d$ (nm),**
**t-plot micropore volume $V_{micro}$ ($cm^3/g$) and surface area $S_{micro}$ ($m^2/g$) of Fe-MOFs and synthesized composites**

| Sample | $S_{BET}$ | $V$ | $d$ | $V_{micro}$ | $S_{micro}$ |
|---|---|---|---|---|---|
| MIL-88b(Fe) [26] | 165 | 0.2 | - | - | - |
| MIL-88b(Fe) [42] | 303 | 0.34 | 2.6 | - | - |
| $NH_2$-MIL-88b(Fe) [42] | 191 | 0.65 | 6.77 | - | - |
| $NH_2$-MIL-88b(Fe) [67] | 14 | - | - | - | - |
| $Fe_3O_4/\gamma-Fe_2O_3@MIL-88b(Fe)$ | 54 | 0.07 | 3.5 | 0.003 | 7.3 |
| $Fe_3O_4/\gamma-Fe_2O_3@NH_2-MIL-88b(Fe)$ | 68 | 0.17 | 8.8 | 0.001 | 5.7 |

*Adsorption and Photocatalytic Degradation*

*Effects of Composite Dosage and pH*

To determine the optimal composite concentration for subsequent studies, the CR removal efficiency Re was initially monitored at different $Fe3O4/\gamma-Fe_2O_3@MIL-88b(Fe)$ and $Fe_3O_4/\gamma-Fe_2O_3@NH_2-MIL-88b(Fe)$ dosages (Fig. 6). As expected, with increasing dosage a gradual rise in CR removal efficiency was observed with an inflection point present at around 15–20 mg for both composites. More importantly, lower dosages increased an error margin for Re values, while elevated Re values at higher dosages limited further assessment of photocatalytic activity. Therefore, an optimal concentration of composite was determined to be 2 g/L, during which a moderate 40–60 % CR removal efficiency was observed.
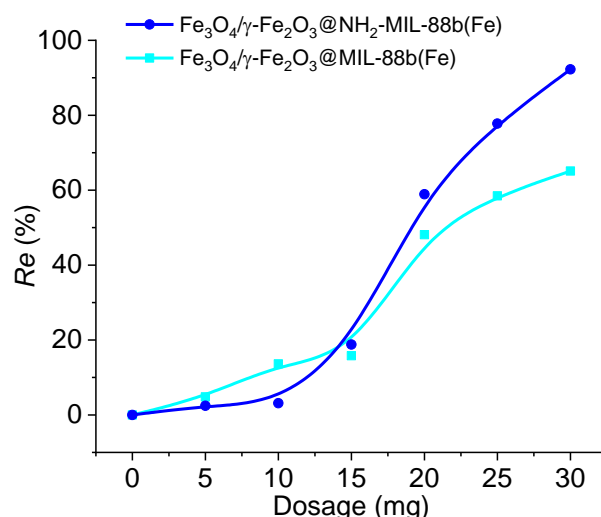
Figure 6. The effect of composite dosage on the CR removal efficiency *Re* for Fe$_3$O$_4$/γ-Fe$_2$O$_3$@MIL-88b(Fe)
and Fe$_3$O$_4$/γ-Fe$_2$O$_3$@NH$_2$-MIL-88b(Fe) composites

To evaluate each composite maximum adsorption capacity *q*, CR removal efficiency *Re* was monitored in the pH range of 5 to 12 for Fe$_3$O$_4$/γ-Fe$_2$O$_3$@MIL-88b(Fe) and Fe$_3$O$_4$/γ-Fe$_2$O$_3$@NH$_2$-MIL-88b(Fe) (Fig. 7). In contrast with Fe$_3$O$_4$/γ-Fe$_2$O$_3$@MIL-88b(Fe), higher *Re* values were generally observed for Fe$_3$O$_4$/γ-Fe$_2$O$_3$@NH$_2$-MIL-88b(Fe), porous structure of which supposedly exhibited better stability due to dispersion interactions between -NH$_2$ groups and was therefore more accessible [69].
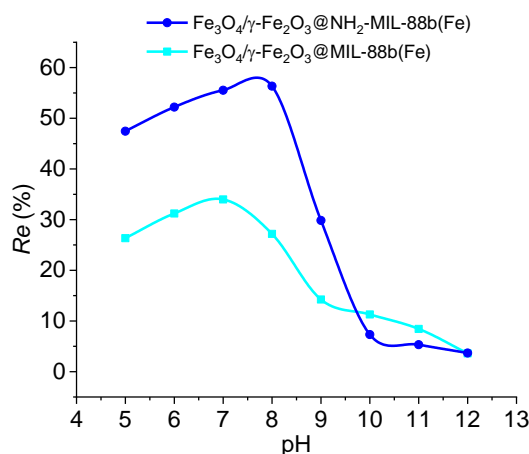


Figure 7. The effect of solution pH on the CR removal efficiency *Re* for Fe$_3$O$_4$/γ-Fe$_2$O$_3$@MIL-88b(Fe)
and Fe$_3$O$_4$/γ-Fe$_2$O$_3$@NH$_2$-MIL-88b(Fe) composites

Additionally, Fe$_3$O$_4$/γ-Fe$_2$O$_3$@MIL-88b(Fe) and Fe$_3$O$_4$/γ-Fe$_2$O$_3$@NH$_2$-MIL-88b(Fe) adsorption capacities peaked at 10.2 mg/g with pH of 7 and 16.9 mg/g with pH of 8, respectively. These maxima occurrence can be explained by composite surface Zeta potential. Reportedly, Zhao X. and colleagues have evaluated that the point of zero charge *pzc* for NH$_2$-MIL-101(Cr) (which partially resembles MIL-88b(Fe) and NH$_2$-MIL-88b(Fe) structures) occurs at slightly basic pH (7.8), whereas at lower pH its surface charges positively [70]. Assuming that *pzc* for Fe$_3$O$_4$/γ-Fe$_2$O$_3$@MIL-88b(Fe) also occurs at slightly basic pH (8), a pH of 7 positively charges composite surface [71], which then electrostatically attracts CR molecules via negatively charged -SO$_3^-$ groups, thus a peak *Re* value is reached. A decrease in *Re* values at acidic pH may be caused by neutral or repelling interactions between positively charged composite surface and CR zwitterions [72] or CR protonated molecules, respectively. Lastly, *Re* values dropped significantly at basic pH possibly due to electrostatic repulsion between negatively charged -SO$_3^-$ groups of CR molecules and -COO$^-$ groups in BDC linkers. Similar assumptions can be made for Fe$_3$O$_4$/γ-Fe$_2$O$_3$@NH$_2$-MIL-88b(Fe) with *pzc* at pH of 9. However, at basic pH donor mesomeric effect, inherent in -NH$_2$ groups, causes *Re* values to diminish faster.

*Adsorption Kinetics and Photocatalytic Activity*

To observe adsorption kinetics and study photocatalytic activity of the composites, a change in CR normalized concentration $C/C_0$ over time t was monitored during photodegradation via $H_2O_2$ and UV irradiation ($H_2O_2$+UV), isolated adsorption (composite) and photocatalytic degradation (composite+$H_2O_2$+UV) for Fe₃O₄/γ-Fe₂O₃@MIL-88b(Fe) and Fe₃O₄/γ-Fe₂O₃@NH₂-MIL-88b(Fe) (Fig. 8). The $H_2O_2$+UV system was the least effective since its removal efficiency Re peaked at 15 %. During isolated adsorption Fe₃O₄/γ-Fe₂O₃@MIL-88b(Fe) and Fe₃O₄/γ-Fe₂O₃@NH₂-MIL-88b(Fe) performed almost identically with Re values reaching 38-44 %. Nevertheless, when each composite, $H_2O_2$ and UV irradiation were utilized simultaneously, Fenton-like reaction occurred [34], which generated highly reactive hydroxyl radicals for CR degradation. As a result, during CR photocatalytic degradation both composite+$H_2O_2$+UV systems demonstrated even higher Re values of 89 % and 95 % for Fe₃O₄/γ-Fe₂O₃@MIL-88b(Fe) and Fe₃O₄/γ-Fe₂O₃@NH₂-MIL-88b(Fe), respectively. Moreover, a higher photocatalytic activity was observed for Fe₃O₄/γ-Fe₂O₃@NH₂-MIL-88b(Fe) with a Re value reaching 88 % in 15 minutes, whereas Fe₃O₄/γ-Fe₂O₃@MIL-88b(Fe) required more than 1.5 hours for Re value to reach 89 %. Supposedly, -NH₂ group increases the electron density on the aryl ring, which stabilizes hole localization at the organic linker, increases photoexcited state lifetime and promotes electron transfer onto metal center in Fe-μ₃-O cluster [73]. Therefore, Fe₃O₄/γ-Fe₂O₃@NH₂-MIL-88b(Fe) generated more hydroxyl radicals and degraded CR faster, than Fe₃O₄/γ-Fe₂O₃@MIL-88b(Fe).
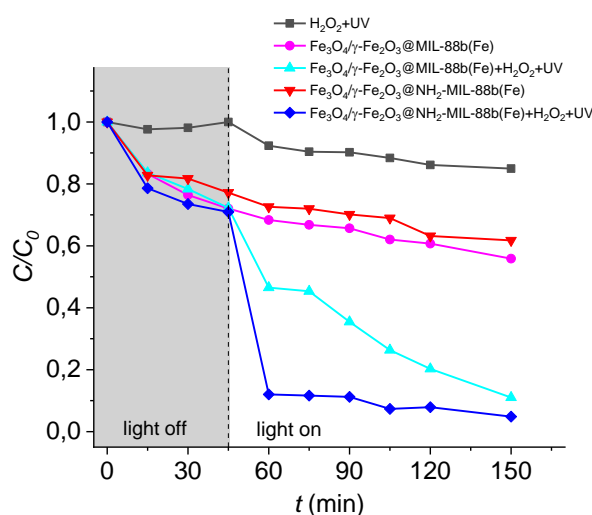


Figure 8. Adsorption kinetics and photocatalytic activity of Fe₃O₄/γ-Fe₂O₃@MIL-88b(Fe) and Fe₃O₄/γ-Fe₂O₃@NH₂-MIL-88b(Fe) composites

To quantify photocatalytic degradation kinetics, the pseudo-first-order model can be implemented:

$$\ln\left(\frac{C}{C_0}\right) = -k \cdot t, \tag{6}$$

where $k$ is photodegradation rate constant. The resulting $k$ values for Fe₃O₄/γ-Fe₂O₃@MIL-88b(Fe) and Fe₃O₄/γ-Fe₂O₃@NH₂-MIL-88b(Fe) were 0.013±0.001 min⁻¹ and 0.023±0.002 min⁻¹, respectively. According to previous studies, $k$ value depends not only on the type of photocatalyst used, but is also highly reliant on the incident photon energy from particular irradiation source. For example, if Rhodamine B was degraded under visible light in presence of MIL-88A(Fe)[74], MIL-88A@GO and MIL-88A@polyacrylate composites [75], the resulting $k$ values were 0.0793 min⁻¹ (natural sunlight), 0.0645 min⁻¹ and 0.0726 min⁻¹ (500W Xe lamp with UV cutoff filter) (Table S1), respectively. When visible light was replaced by UV irradiation, the $k$ value for MIL-88A(Fe) quadrupled [76], reaching 0.461 min⁻¹ (9W UVA lamp). Therefore, in comparison with homogeneous Fenton [77] and heterogeneous SnO₂–Fe₃O₄ [78] and MgFe₂O₄ [79] systems with UV irradiation (Table S1), Fe₃O₄/γ-Fe₂O₃@MIL-88b(Fe) and Fe₃O₄/γ-Fe₂O₃@NH₂-MIL-88b(Fe) were acceptable photocatalysts, since they exhibited similar rate constants and higher *Re* values.

*Cyclability of Composites*

To analyze the possibility of Fe-MOF coating peeling off from Fe₃O₄/γ-Fe₂O₃ particles surface, we decided to carry out three consecutive photocatalysis cycles in the same conditions (Fig. 9). After first and sec-

ond photocatalysis cycles each composite was magnetically separated from the solution, washed with distilled water (200 mL) and dried in a vacuum ($10^{-3}$ Torr, 50 °C. 5 h). As a result, $Fe_3O_4/\gamma$-$Fe_2O_3$@MIL-88b(Fe) demonstrated poor stability since *Re* decreased from 89 % in first cycle to 29 % in third cycle (Fig. 9). In contrast with $Fe_3O_4/\gamma$-$Fe_2O_3$@MIL-88b(Fe), a smaller drop in photocatalytic activity was observed for $Fe_3O_4/\gamma$-$Fe_2O_3$@NH$_2$-MIL-88b(Fe) composite, which resulted in Re decreasing from 95 % in first cycle to 69 % in third cycle (Fig. 9), suggesting slower peeling of NH$_2$-MIL-88b(Fe). This observation was additionally confirmed by comparing FTIR spectra of dried composites before each cycle, where a drop in Fe-bound carboxylate group bands (1376-1561 cm$^{-1}$) intensity for $Fe_3O_4/\gamma$-$Fe_2O_3$@MIL-88b(Fe) composite (Fig. S3a) was more rapid than that of $Fe_3O_4/\gamma$-$Fe_2O_3$@NH$_2$-MIL-88b(Fe) (Fig. S3b). Ultimately, $Fe_3O_4/\gamma$-$Fe_2O_3$@NH$_2$-MIL-88b(Fe) composite has demonstrated better cyclability than $Fe_3O_4/\gamma$-$Fe_2O_3$@MIL-88b(Fe).
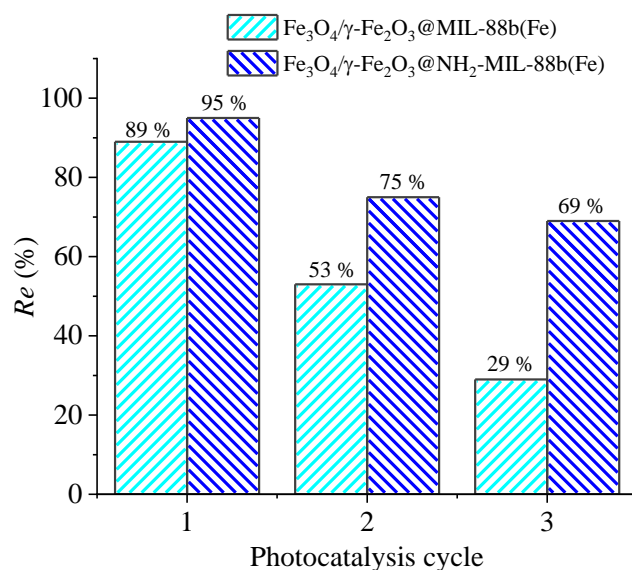


Figure 9. Removal efficiency Re of CR dye for $Fe_3O_4/\gamma$-$Fe_2O_3$@MIL-88b(Fe)
and $Fe_3O_4/\gamma$-$Fe_2O_3$@NH$_2$-MIL-88b(Fe) composites during three consecutive photocatalysis cycles

## *Conclusions*

In this study, $Fe_3O_4/Fe_2O_3$@MIL-88b(Fe) and $Fe_3O_4/\gamma$-$Fe_2O_3$@NH$_2$-MIL-88b(Fe) composites were obtained, where $Fe_3O_4/\gamma$-$Fe_2O_3$ particles enabled magnetic separation, and Fe-MOF coating exhibited photocatalytic activity. Fe-MOFs were constructed through rational approach of utilizing pre-synthesized $Fe_3$-$\mu_3$-O acetate clusters as secondary building units, geometry of which strictly determined the coordination of BDC or NH$_2$-BDC linkers. The elemental analysis and FTIR spectra confirmed the presence of both $Fe_3O_4/\gamma$-$Fe_2O_3$ particles and Fe-MOFs in composites structure. Using composites XRD patterns, the $Fe_3O_4$ content was determined to be 22.7 wt. % and 72.2 wt. % for $Fe_3O_4/\gamma$-$Fe_2O_3$ particles in $Fe_3O_4/\gamma$-$Fe_2O_3$@MIL-88b(Fe) and $Fe_3O_4/\gamma$-$Fe_2O_3$@NH$_2$-MIL-88b(Fe), respectively. Magnetization curves of $Fe_3O_4/\gamma$-$Fe_2O_3$@MIL-88b(Fe) and $Fe_3O_4/\gamma$-$Fe_2O_3$@NH$_2$-MIL-88b(Fe) specified saturation magnetization $M_s$ of 14–19 emu/g, remanent magnetization $M_r$ of 0.9-1.2 emu/g and coercivity $H_c$ of 33 Oe. All these values were lower than those of isolated $Fe_3O_4$ and $\gamma$-$Fe_2O_3$ particles, but the $M_s$ composites values were sufficient for magnetic separation. TGA profiles for $Fe_3O_4/\gamma$-$Fe_2O_3$@MIL-88b(Fe) and $Fe_3O_4/\gamma$-$Fe_2O_3$@NH$_2$-MIL-88b(Fe) exhibited three main weight loss steps, where every second step had the maximum weight loss rate above 300 °C and was attributed to the decarboxylation of -COO$^-$ groups in organic linkers. Both $Fe_3O_4/\gamma$-$Fe_2O_3$@MIL-88b(Fe) and $Fe_3O_4/\gamma$-$Fe_2O_3$@NH$_2$-MIL-88b(Fe) exhibited type IV nitrogen adsorption-desorption isotherms, suggesting Fe-MOFs mesoporous structure, and their $S_{BET}$ values were 54 and 68 m$^2$/g, respectively. In contrast with $Fe_3O_4/\gamma$-$Fe_2O_3$@MIL-88b(Fe), higher Re values were generally observed for $Fe_3O_4/\gamma$-$Fe_2O_3$@NH$_2$-MIL-88b(Fe), porous structure of which supposedly exhibited better stability due to dispersion interactions between -NH$_2$ groups and was therefore more accessible. Additionally, $Fe_3O_4/\gamma$-$Fe_2O_3$@MIL-88b(Fe) and $Fe_3O_4/\gamma$-$Fe_2O_3$@NH$_2$-MIL-88b(Fe) adsorption capacities peaked at 10.2 mg/g with pH of 7 and 16.9 mg/g with pH of 8, respectively. When each composite, H$_2$O$_2$ and UV irradiation were utilized simultaneously, Fenton-like

reaction occurred, which generated highly reactive hydroxyl radicals for CR degradation. As a result, during CR photocatalytic degradation high *Re* values of 89 % and 95 % were achieved for $Fe_3O_4/\gamma$-$Fe_2O_3$@MIL-88b(Fe) and $Fe_3O_4/\gamma$-$Fe_2O_3$@$NH_2$-MIL-88b(Fe), respectively. Moreover, a higher photocatalytic activity was observed for $Fe_3O_4/\gamma$-$Fe_2O_3$@$NH_2$-MIL-88b(Fe), supposedly, due to -$NH_2$ group increasing the electron density on the aryl ring, which stabilized hole localization at the organic linker, increased photoexcited state lifetime and promoted electron transfer onto metal center in $Fe_3$-$\mu_3$-O cluster. Therefore, $Fe_3O_4/\gamma$-$Fe_2O_3$@$NH_2$-MIL-88b(Fe) generated more hydroxyl radicals and degraded CR faster, than $Fe_3O_4/\gamma$-$Fe_2O_3$@MIL-88b(Fe). Finally, when compared to homogeneous Fenton and $SnO_2$–$Fe_3O_4$ and $MgFe_2O_4$ heterogeneous systems, $Fe_3O_4/\gamma$-$Fe_2O_3$@MIL-88b(Fe) and $Fe_3O_4/\gamma$-$Fe_2O_3$@$NH_2$-MIL-88b(Fe) exhibited similar rate constants and higher Re values. Ultimately, $Fe_3O_4/\gamma$-$Fe_2O_3$@$NH_2$-MIL-88b(Fe) composite has demonstrated better cyclability than $Fe_3O_4/\gamma$-$Fe_2O_3$@MIL-88b(Fe).

## *Supporting Information*

The Supporting Information is available free at https://ejc.buketov.edu.kz/index.php/ejc/article/view/130/93

## *Author Information\**

---

*\*The authors' names are presented in the following order: First Name, Middle Name and Last Name*

*Vladislav Lvovich Sidorov* — Graduate student of Department of Fundamental Physical and Chemical Engineering, Lomonosov Moscow State University, 119991, Moscow, Russia; Laboratory Assistant, Federal Research Center of Problems of Chemical Physics and Medicinal Chemistry, Russian Academy of Sciences, 142432, Chernogolovka, Moscow region, Russia; e-mail: bobik_132@mail.ru

*Rose Kurmangalievna Baimuratova (corresponding author)* — Candidate of Chemical Sciences, Junior Researcher, Federal Research Center of Problems of Chemical Physics and Medicinal Chemistry, Russian Academy of Sciences, 142432, Chernogolovka, Moscow region, Russia; e-mail: roz_baz@mail.ru; https://orcid.org/0000-0002-8389-6871

*Denis Vladimirovich Korchagin* — Candidate of Chemical Sciences, Leading Researcher, Federal Research Center of Problems of Chemical Physics and Medicinal Chemistry, Russian Academy of Sciences, 142432, Chernogolovka, Moscow region, Russia; e-mail: korden@icp.ac.ru; https://orcid.org/0000-0002-0199-1382

*Andrey Vladimirovich Ivanov* — Candidate of Chemical Sciences, Senior Researcher, Federal Research Center of Problems of Chemical Physics and Medicinal Chemistry, Russian Academy of Sciences, 142432, Chernogolovka, Moscow region, Russia; e-mail: dzhardim@icp.ac.ru

*Kamila Asylbekovna Kydralieva* — Doctor of Chemical Sciences, Professor Employment, Moscow Aviation Institute (National Research University), 125993, Moscow, Russia; e-mail: kydralievaka@mai.ru; https://orcid.org/0000-0002-4596-4140

*Gulzhian Iskakovna Dzhardimalieva* — Doctor of Chemical Sciences, Head of Laboratory of Metallopolymers, Federal Research Center of Problems of Chemical Physics and Medicinal Chemistry, Russian Academy of Sciences, 142432, Chernogolovka, Moscow region, Russia; e-mail: g_dzhardim@mail.ru; https://orcid.org/0000-0002-4727-8910

## *Author Contributions*

The manuscript was written through contributions of all authors. All authors have given approval to the final version of the manuscript. CRediT: **Vladislav Lvovich Sidorov**: investigation, methodology, visualization, writing — original draft, formal analyses; **Rose Kurmangalievna Baimuratova**: investigation, conceptualization, validation, writing — original draft; **Denis Vladimirovich Korchagin**: investigation, software, formal analyses; **Andrey Vladimirovich Ivanov**: investigation, methodology, data curation; **Kamila**

**Asylbekovna Kydralieva**: methodology, data curation; **Gulzhian Iskakovna Dzhardimalieva**: conceptualization, methodology, writing — review & editing, supervision.

*Conflicts of Interest*

All authors declare that they have no conflicts of interest.

## References

1 Ihmels, H. (2019). Dyes in modern organic chemistry. *Beilstein Journal of Organic Chemistry*, *15*, 2798–2800. https://doi.org/10.3762/bjoc.15.272

2 Qadri, R., & Faiq, M. A. (2020). Freshwater Pollution: Effects on Aquatic Life and Human Health. In: Qadri, H., Bhat, R., Mehmood, M., Dar, G. (eds). *Fresh Water Pollution Dynamics and Remediation* (Pp. 15–26). Springer Singapore. https://doi.org/10.1007/978-981-13-8277-2_2

3 Pizzicato, B., Pacifico, S., Cayuela, D., Mijas, G., & Riba-Moliner, M. (2023). Advancements in Sustainable Natural Dyes for Textile Applications: A Review. *Molecules*, *28*(16), 5954. https://doi.org/10.3390/molecules28165954

4 Murcia, M. D., Gómez, M., Gómez, E., Gómez, J. L., & Christofi, N. (2011). Photodegradation of congo red using XeBr, KrCl and Cl2 barrier discharge excilamps: A kinetics study. *Desalination*, *281*, 364–371. https://doi.org/10.1016/j.desal.2011.08.011

5 Jin, X.-C., Liu, G.-Q., Xu, Z.-H., & Tao, W.-Y. (2007). Decolorization of a dye industry effluent by Aspergillus fumigatus XC6. *Applied Microbiology and Biotechnology*, *74*(1), 239–243. https://doi.org/10.1007/s00253-006-0658-1

6 Swan, N. B., & Zaini, M. A. A. (2019). Adsorption of Malachite Green and Congo Red Dyes from Water: Recent Progress and Future Outlook. *Ecological Chemistry and Engineering S*, *26*(1), 119–132. https://doi.org/10.1515/eces-2019-0009

7 Hanafi, M. F., & Sapawe, N. (2020). A review on the current techniques and technologies of organic pollutants removal from water/wastewater. *Materials Today: Proceedings*, *31*, A158–A165. https://doi.org/10.1016/j.matpr.2021.01.265

8 Kokkinos, P., Venieri, D., & Mantzavinos, D. (2021). Advanced Oxidation Processes for Water and Wastewater Viral Disinfection. A Systematic Review. *Food and Environmental Virology*, *13*(3), 283–302. https://doi.org/10.1007/s12560-021-09481-1

9 Mahmoodi, N. M., Arami, M., Limaee, N. Y., & Tabrizi, N. S. (2006). Kinetics of heterogeneous photocatalytic degradation of reactive dyes in an immobilized TiO2 photocatalytic reactor. *Journal of Colloid and Interface Science*, *295*(1), 159–164. https://doi.org/10.1016/j.jcis.2005.08.007

10 Holkar, C. R., Jadhav, A. J., Pinjari, D. V., Mahamuni, N. M., & Pandit, A. B. (2016). A critical review on textile wastewater treatments: Possible approaches. *Journal of Environmental Management*, *182*, 351–366. https://doi.org/10.1016/j.jenvman.2016.07.090

11 Perazolli, L., Nuñez, L., Silva, M. R. A. D., Pegler, G. F., Costalonga, A. G. C., Gimenes, R., Kondo, M. M., & Bertochi, M. A. Z. (2011). TiO<; sub>2<;/sub>/CuO Films Obtained by Citrate Precursor Method for Photocatalytic Application. *Materials Sciences and Applications*, *02*(06), 564–571. https://doi.org/10.4236/msa.2011.26075

12 Mishra, N., Reddy, R., Kuila, A., Rani, A., Nawaz, A., & Pichiah, S. (2017). A Review on Advanced Oxidation Processes for Effective Water Treatment. *Current World Environment*, *12*(3), 469–489. https://doi.org/10.12944/CWE.12.3.02

13 Wang, L., Yun, J., Zhang, H., Si, J., Fang, X., & Shao, L. (2021). Degradation of Bisphenol A by ozonation in rotating packed bed: Effects of operational parameters and co-existing chemicals. *Chemosphere*, *274*, 129769. https://doi.org/10.1016/j.chemosphere.2021.129769

14 Pędziwiatr, P., Mikołajczyk, F., Zawadzki, D., Mikołajczyk, K., & Bedka, A. (2018). Decomposition of hydrogen peroxide— Kinetics and review of chosen catalysts. *Acta Innovations*, *26*, 45–52. https://doi.org/10.32933/ActaInnovations.26.5

15 Liu, B., Chen, B., & Zhang, B. (2017). Oily Wastewater Treatment by Nano-TiO₂ -Induced Photocatalysis: Seeking more efficient and feasible solutions. *IEEE Nanotechnology Magazine*, *11*(3), 4–15. https://doi.org/10.1109/MNANO.2017.2708818

16 O'Dowd, K., & Pillai, S. C. (2020). Photo-Fenton disinfection at near neutral pH: Process, parameter optimization and recent advances. *Journal of Environmental Chemical Engineering*, *8*(5), 104063. https://doi.org/10.1016/j.jece.2020.104063

17 Gupta, S. M., & Tripathi, M. (2011). A review of TiO₂ nanoparticles. *Chinese Science Bulletin*, *56*(16), 1639–1657. https://doi.org/10.1007/s11434-011-4476-1

18 López, Y. C., Viltres, H., Gupta, N. K., Acevedo-Peña, P., Leyva, C., Ghaffari, Y., Gupta, A., Kim, S., Bae, J., & Kim, K. S. (2021). Transition metal-based metal–organic frameworks for environmental applications: A review. *Environmental Chemistry Letters*, *19*(2), 1295–1334. https://doi.org/10.1007/s10311-020-01119-1

19 Batten, S. R., Champness, N. R., Chen, X. -M., Garcia-Martinez, J., Kitagawa, S., Öhrström, L., O'Keeffe, M., Paik Suh, M., & Reedijk, J. (2013). Terminology of metal–organic frameworks and coordination polymers (IUPAC Recommendations 2013). *Pure and Applied Chemistry*, *85*(8), 1715–1724. https://doi.org/10.1351/PAC-REC-12-11-20

20 Wang, D., Huang, R., Liu, W., Sun, D., & Li, Z. (2014). Fe-Based MOFs for Photocatalytic CO₂ Reduction: Role of Coordination Unsaturated Sites and Dual Excitation Pathways. *ACS Catalysis*, *4*(12), 4254–4260. https://doi.org/10.1021/cs501169t

21 Shanmugam, M., Agamendran, N., Sekar, K., & Natarajan, T. S. (2023). Metal–organic frameworks (MOFs) for energy production and gaseous fuel and electrochemical energy storage applications. *Physical Chemistry Chemical Physics*, *25*(44), 30116–30144. https://doi.org/10.1039/D3CP04297A

22  Park, J., Agrawal, M., Sava Gallis, D. F., Harvey, J. A., Greathouse, J. A., & Sholl, D. S. (2020). Impact of intrinsic framework flexibility for selective adsorption of sarin in non-aqueous solvents using metal–organic frameworks. *Physical Chemistry Chemical Physics*, *22*(11), 6441–6448. https://doi.org/10.1039/C9CP06788D

23  Shi, L., Wang, T., Zhang, H., Chang, K., & Ye, J. (2015). Electrostatic Self-Assembly of Nanosized Carbon Nitride Nanosheet onto a Zirconium Metal–Organic Framework for Enhanced Photocatalytic $CO_2$ Reduction. *Advanced Functional Materials*, *25*(33), 5360–5367. https://doi.org/10.1002/adfm.201502253

24  Ma, Y., Lu, Y., Hai, G., Dong, W., Li, R., Liu, J., & Wang, G. (2020). Bidentate carboxylate linked TiO2 with NH2-MIL-101(Fe) photocatalyst: A conjugation effect platform for high photocatalytic activity under visible light irradiation. *Science Bulletin*, *65*(8), 658–669. https://doi.org/10.1016/j.scib.2020.02.001

25  Liu, Y., Yang, Y., Sun, Q., Wang, Z., Huang, B., Dai, Y., Qin, X., & Zhang, X. (2013). Chemical Adsorption Enhanced $CO_2$ Capture and Photoreduction over a Copper Porphyrin Based Metal Organic Framework. *ACS Applied Materials & Interfaces*, *5*(15), 7654–7658. https://doi.org/10.1021/am4019675

26  Gao, C., Chen, S., Quan, X., Yu, H., & Zhang, Y. (2017). Enhanced Fenton-like catalysis by iron-based metal organic frameworks for degradation of organic pollutants. *Journal of Catalysis*, *356*, 125–132. https://doi.org/10.1016/j.jcat.2017.09.015

27  Laurier, K. G. M., Vermoortele, F., Ameloot, R., De Vos, D. E., Hofkens, J., & Roeffaers, M. B. J. (2013). Iron(III)-Based Metal–Organic Frameworks As Visible Light Photocatalysts. *Journal of the American Chemical Society*, *135*(39), 14488–14491. https://doi.org/10.1021/ja405086e

28  Hou, S., Wu, Y., Feng, L., Chen, W., Wang, Y., Morlay, C., & Li, F. (2018). Green synthesis and evaluation of an iron-based metal–organic framework MIL-88B for efficient decontamination of arsenate from water. *Dalton Transactions*, *47*(7), 2222–2231. https://doi.org/10.1039/C7DT03775A

29  Yue, X., Guo, W., Li, X., Gao, X., & Zhang, G. (2017). Preparation of Efficient BiOBr/MIL-88B(Fe) Composites with Enhanced Photocatalytic Activities. *Water Environment Research*, *89*(7), 614–621. https://doi.org/10.2175/106143017X14839994522821

30  Gecgel, C., Simsek, U. B., Gozmen, B., & Turabik, M. (2019). Comparison of MIL-101(Fe) and amine-functionalized MIL-101(Fe) as photocatalysts for the removal of imidacloprid in aqueous solution. *Journal of the Iranian Chemical Society*, *16*(8), 1735–1748. https://doi.org/10.1007/s13738-019-01647-w

31  Guo, H., Niu, B., Wu, X., Zhang, Y., & Ying, S. (2019). Effective removal of 2,4,6-trinitrophenol over hexagonal metal–organic framework $NH_2$-MIL-88B(Fe). *Applied Organometallic Chemistry*, *33*(1), e4580. https://doi.org/10.1002/aoc.4580

32  Alluhaybi, A. A., Alharbi, A., Alshammari, K. F., & El-Desouky, M. G. (2023). Efficient Adsorption and Removal of the Herbicide 2,4-Dichlorophenylacetic Acid from Aqueous Solutions Using MIL-88(Fe)-$NH_2$. *ACS Omega*, *8*(43), 40775–40784. https://doi.org/10.1021/acsomega.3c05818

33  Howarth, A. J., Liu, Y., Li, P., Li, Z., Wang, T. C., Hupp, J. T., & Farha, O. K. (2016). Chemical, thermal and mechanical stabilities of metal–organic frameworks. *Nature Reviews Materials*, *1*(3), 15018. https://doi.org/10.1038/natrevmats.2015.18

34  Chen, M.-L., Lu, T.-H., Long, L.-L., Xu, Z., Ding, L., & Cheng, Y.-H. (2021). NH2-Fe-MILs for effective adsorption and Fenton-like degradation of imidacloprid: Removal performance and mechanism investigation. *Environmental Engineering Research*, *27*(2), 200702–0. https://doi.org/10.4491/eer.2020.702

35  Li, Y., Jiang, J., Fang, Y., Cao, Z., Chen, D., Li, N., Xu, Q., & Lu, J. (2018). TiO2 Nanoparticles Anchored onto the Metal–Organic Framework NH2-MIL-88B(Fe) as an Adsorptive Photocatalyst with Enhanced Fenton-like Degradation of Organic Pollutants under Visible Light Irradiation. *ACS Sustainable Chemistry & Engineering*, *6*(12), 16186–16197. https://doi.org/10.1021/acssuschemeng.8b02968

36  Mateo, D., Santiago-Portillo, A., Albero, J., Navalón, S., Alvaro, M., & García, H. (2019). Long-Term Photostability in Terephthalate Metal–Organic Frameworks. *Angewandte Chemie International Edition*, *58*(49), 17843–17848. https://doi.org/10.1002/anie.201911600

37  Peralta, M. E., Ocampo, S., Funes, I. G., Onaga Medina, F., Parolo, M. E., & Carlos, L. (2020). Nanomaterials with Tailored Magnetic Properties as Adsorbents of Organic Pollutants from Wastewaters. *Inorganics*, *8*(4), 24. https://doi.org/10.3390/inorganics8040024

38  Hernandez, J. S. T., Aragón-Muriel, A., Corrales Quintero, W., Castro Velásquez, J. C., Salazar-Camacho, N. A., Pérez Alcázar, G. A., & Tabares, J. A. (2022). Characterization of Fe3O4 Nanoparticles for Applications in Catalytic Activity in the Adsorption/Degradation of Methylene Blue and Esterification. *Molecules*, *27*(24), 8976. https://doi.org/10.3390/molecules27248976

39  Hermanek, M., Zboril, R., Medrik, I., Pechousek, J., & Gregor, C. (2019). Retraction of "Catalytic Efficiency of Iron(III) Oxides in Decomposition of Hydrogen Peroxide: Competition between the Surface Area and Crystallinity of Nanoparticles". *Journal of the American Chemical Society*, *141*(51), 20566–20566. https://doi.org/10.1021/jacs.9b03677

40  Liu, M., Ye, Y., Ye, J., Gao, T., Wang, D., Chen, G., & Song, Z. (2023). Recent Advances of Magnetite (Fe₃O₄)-Based Magnetic Materials in Catalytic Applications. *Magnetochemistry*, *9*(4), 110. https://doi.org/10.3390/magnetochemistry9040110

41  Zhang, C.-F., Qiu, L.-G., Ke, F., Zhu, Y.-J., Yuan, Y.-P., Xu, G.-S., & Jiang, X. (2013). A novel magnetic recyclable photocatalyst based on a core–shell metal–organic framework Fe₃O₄@MIL-100(Fe) for the decolorization of methylene blue dye. *Journal of Materials Chemistry A*, *1*(45), 14329. https://doi.org/10.1039/c3ta13030d

42  Baimuratova, R. K., Zhinzhilo, V. A., Uflyand, I. E., Dmitriev, A. I., Zhidkov, M. V., Ovanesyan, N. S., Kugabaeva, G. D., & Dzhardimalieva, G. I. (2023). Low-Temperature Synthesis of Metal–Organic Coordination Polymers Based on Oxo-centered Iron Complexes: Magnetic and Adsorption Properties. *Russian Journal of Physical Chemistry A*, *97*(4), 735–748. https://doi.org/10.1134/S0036024423040064

43 Sapianik, A. A., Kiskin, M. A., Kovalenko, K. A., Samsonenko, D. G., Dybtsev, D. N., Audebrand, N., Sun, Y., & Fedin, V. P. (2019). Rational synthesis and dimensionality tuning of MOFs from preorganized heterometallic molecular complexes. *Dalton Trans.*, *48*(11), 3676–3686. https://doi.org/10.1039/C8DT05136D

44 Wongsakulphasatch, S., Nouar, F., Rodriguez, J., Scott, L., Le Guillouzer, C., Devic, T., Horcajada, P., Grenèche, J. -M., Llewellyn, P. L., Vimont, A., Clet, G., Daturi, M., & Serre, C. (2015). Direct accessibility of mixed-metal (III / II) acid sites through the rational synthesis of porous metal carboxylates. *Chemical Communications*, *51*(50), 10194–10197. https://doi.org/10.1039/C5CC02550H

45 Peng, L., Asgari, M., Mieville, P., Schouwink, P., Bulut, S., Sun, D. T., Zhou, Z., Pattison, P., van Beek, W., & Queen, W. L. (2017). Using Predefined M 3 (μ 3 -O) Clusters as Building Blocks for an Isostructural Series of Metal–Organic Frameworks. *ACS Applied Materials & Interfaces*, *9*(28), 23957–23966. https://doi.org/10.1021/acsami.7b06041

46 Elmore, W. C. (1938). Ferromagnetic Colloid for Studying Magnetic Structures. *Physical Review*, *54*(4), 309–310. https://doi.org/10.1103/PhysRev.54.309

47 Devi, L., Kumar, S., & Reddy, K. (2009). Photo fenton like process $Fe^{3+}/(NH_4)_2S_2O_8/UV$ for the degradation of Di azo dye congo red using low iron concentration. *Open Chemistry*, *7*(3), 468–477. https://doi.org/10.2478/s11532-009-0036-9

48 Yadav, S., Dixit, R., Sharma, S., Dutta, S., Solanki, K., & Sharma, R. K. (2021). Magnetic metal–organic framework composites: Structurally advanced catalytic materials for organic transformations. *Materials Advances*, *2*(7), 2153–2187. https://doi.org/10.1039/D0MA00982B

49 Huang, L. (2003). Synthesis, morphology control, and properties of porous metal–organic coordination polymers. *Microporous and Mesoporous Materials*, *58*(2), 105–114. https://doi.org/10.1016/S1387-1811(02)00609-1

50 Bennett, T. D., & Cheetham, A. K. (2014). Amorphous Metal–Organic Frameworks. *Accounts of Chemical Research*, *47*(5), 1555–1562. https://doi.org/10.1021/ar5000314

51 Yaghi, O. M., O'Keeffe, M., Ockwig, N. W., Chae, H. K., Eddaoudi, M., & Kim, J. (2003). Reticular synthesis and the design of new materials. *Nature*, *423*(6941), 705–714.

52 Ockwig, N. W., Delgado-Friedrichs, O., O'Keeffe, M., & Yaghi, O. M. (2005). Reticular Chemistry: Occurrence and Taxonomy of Nets and Grammar for the Design of Frameworks. *Accounts of Chemical Research*, *38*(3), 176–182. https://doi.org/10.1021/ar0200221

53 Zhang, S., Zhuo, Y., Ezugwu, C. I., Wang, C., Li, C., & Liu, S. (2021). Synergetic Molecular Oxygen Activation and Catalytic Oxidation of Formaldehyde over Defective MIL-88B(Fe) Nanorods at Room Temperature. *Environmental Science & Technology*, *55*(12), 8341–8350. https://doi.org/10.1021/acs.est.1c01277

54 Nakamoto, K. (2009). *Infrared and Raman spectra of inorganic and coordination compounds* (6th ed). Wiley.

55 Batista, M. A., Costa, A. C. S. D., Souza Junior, I. G. D., & Bigham, J. M. (2008). Cristallochemical characterization of synthetic Zn-substituted maghemites (g-Fe2-xZn xO3). *Revista Brasileira de Ciência do Solo*, *32*(2), 561–568. https://doi.org/10.1590/S0100-06832008000200011

56 Gorski, C. A., & Scherer, M. M. (2010). Determination of nanoparticulate magnetite stoichiometry by Mossbauer spectroscopy, acidic dissolution, and powder X-ray diffraction: A critical review. *American Mineralogist*, *95*(7), 1017–1026. https://doi.org/10.2138/am.2010.3435

57 Pallach, R., Keupp, J., Terlinden, K., Frentzel-Beyme, L., Kloß, M., Machalica, A., Kotschy, J., Vasa, S. K., Chater, P. A., Sternemann, C., Wharmby, M. T., Linser, R., Schmid, R., & Henke, S. (2021). Frustrated flexibility in metal-organic frameworks. *Nature Communications*, *12*(1), 4097. https://doi.org/10.1038/s41467-021-24188-4

58 Horcajada, P., Serre, C., Maurin, G., Ramsahye, N. A., Balas, F., Vallet-Regí, M., Sebban, M., Taulelle, F., & Férey, G. (2008). Flexible Porous Metal-Organic Frameworks for a Controlled Drug Delivery. *Journal of the American Chemical Society*, *130*(21), 6774–6780. https://doi.org/10.1021/ja710973k

59 Schneemann, A., Bon, V., Schwedler, I., Senkovska, I., Kaskel, S., & Fischer, R. A. (2014). Flexible metal–organic frameworks. *Chem. Soc. Rev.*, *43*(16), 6062–6096. https://doi.org/10.1039/C4CS00101J

60 Pham, M.-H., Vuong, G.-T., Vu, A.-T., & Do, T.-O. (2011). Novel Route to Size-Controlled Fe–MIL-88B–NH 2 Metal–Organic Framework Nanocrystals. *Langmuir*, *27*(24), 15261–15267. https://doi.org/10.1021/la203570h

61 Ma, M., Bétard, A., Weber, I., Al-Hokbany, N. S., Fischer, R. A., & Metzler-Nolte, N. (2013). Iron-Based Metal–Organic Frameworks MIL-88B and NH2-MIL-88B: High Quality Microwave Synthesis and Solvent-Induced Lattice "Breathing". *Crystal Growth & Design*, *13*(6), 2286–2291. https://doi.org/10.1021/cg301738p

62 Mellot-Draznieks, C., Serre, C., Surblé, S., Audebrand, N., & Férey, G. (2005). Very Large Swelling in Hybrid Frameworks: A Combined Computational and Powder Diffraction Study. *Journal of the American Chemical Society*, *127*(46), 16273–16278. https://doi.org/10.1021/ja054900x

63 Ye, Z., Zhang, W., Lanzalaco, S., Zhao, L., Sirés, I., Xia, P., Zhai, J., & He, Q. (2023). Ultra-uniform MIL-88B(Fe)/Fe3S4 hybrids engineered by partial sulfidation to boost catalysis in electro-Fenton treatment of micropollutants: Experimental and mechanistic insights. *Chemical Engineering Journal*, *455*, 140757. https://doi.org/10.1016/j.cej.2022.140757

64 Kicheeva, A. G., Sushko, E. S., Bondarenko, L. S., Kydralieva, K. A., Pankratov, D. A., Tropskaya, N. S., Dzeranov, A. A., Dzhardimalieva, G. I., Zarrelli, M., & Kudryasheva, N. S. (2023). Functionalized Magnetite Nanoparticles: Characterization, Bioeffects, and Role of Reactive Oxygen Species in Unicellular and Enzymatic Systems. *International Journal of Molecular Sciences*, *24*(2), 1133. https://doi.org/10.3390/ijms24021133

65 Schwaminger, S. P., Bauer, D., Fraga-García, P., Wagner, F. E., & Berensmeier, S. (2017). Oxidation of magnetite nanoparticles: Impact on surface and crystal properties. *CrystEngComm*, *19*(2), 246–255. https://doi.org/10.1039/C6CE02421A

66 Shokrollahi, H. (2017). A review of the magnetic properties, synthesis methods and applications of maghemite. *Journal of Magnetism and Magnetic Materials*, *426*, 74–81. https://doi.org/10.1016/j.jmmm.2016.11.033

67 Tran, L. T., Dang, H. T. M., Tran, H. V., Hoang, G. T. L., & Huynh, C. D. (2023). MIL-88B(Fe)-NH₂: An amine-functionalized metal–organic framework for application in a sensitive electrochemical sensor for $Cd^{2+}$, $Pb^{2+}$, and $Cu^{2+}$ ion detection. *RSC Advances*, *13*(32), 21861–21872. https://doi.org/10.1039/D3RA02828C

68 Zhao, Q., Zhang, L., Wang, X., Jia, X., Xu, P., Zhao, M., & Dai, R. (2019). Simultaneous efficient adsorption and photocatalytic degradation of methylene blue over iron(III)-based metal–organic frameworks: A comparative study. *Transition Metal Chemistry*, *44*(8), 789–797. https://doi.org/10.1007/s11243-019-00349-9

69 Rodenas, T., Van Dalen, M., García-Pérez, E., Serra-Crespo, P., Zornoza, B., Kapteijn, F., & Gascon, J. (2014). Visualizing MOF Mixed Matrix Membranes at the Nanoscale: Towards Structure-Performance Relationships in $CO_2$/$CH_4$ Separation Over NH₂-MIL-53(Al)@PI. *Advanced Functional Materials*, *24*(2), 249–256. https://doi.org/10.1002/adfm.201203462

70 Zhao, X., Zheng, M., Gao, X., Gao, Z., & Huang, H. (2020). Construction of an anionic porous framework via a post-synthesis strategy to regulate the adsorption behavior of organic pollutants. *Journal of Materials Science*, *55*(30), 14751–14760. https://doi.org/10.1007/s10853-020-05043-1

71 Taherzade, S. D., Abbasichaleshtori, M., & Soleimannejad, J. (2022). Efficient and ecofriendly cellulose-supported MIL-100(Fe) for wastewater treatment. *RSC Advances*, *12*(15), 9023–9035. https://doi.org/10.1039/D1RA08949H

72 Fu, Y., & Viraraghavan, T. (2002). Removal of Congo Red from an aqueous solution by fungus Aspergillus niger. *Advances in Environmental Research*, *7*(1), 239–247. https://doi.org/10.1016/S1093-0191(01)00123-X

73 Andrade, P. H. M., Ahouari, H., Volkringer, C., Loiseau, T., Vezin, H., Hureau, M., & Moissette, A. (2023). Electron-Donor Functional Groups, Band Gap Tailoring, and Efficient Charge Separation: Three Keys To Improve the Gaseous Iodine Uptake in MOF Materials. *ACS Applied Materials & Interfaces*, *15*(25), 31032–31048. https://doi.org/10.1021/acsami.3c04955

74 Viswanathan, V. P., Mathew, S. V., Dubal, D. P., Adarsh, N. N., & Mathew, S. (2020). Exploring the Effect of Morphologies of Fe(III) Metal-Organic Framework MIL-88A(Fe) on the Photocatalytic Degradation of Rhodamine B. *ChemistrySelect*, *5*(25), 7534–7542. https://doi.org/10.1002/slct.202001670

75 Xue, B., Du, L., Jin, J., Meng, H., & Mi, J. (2021). In situ growth of MIL-88A into polyacrylate and its application in highly efficient photocatalytic degradation of organic pollutants in water. *Applied Surface Science*, *564*, 150404. https://doi.org/10.1016/j.apsusc.2021.150404

76 Andrew Lin, K.-Y., Chang, H.-A., & Hsu, C.-J. (2015). Iron-based metal organic framework, MIL-88A, as a heterogeneous persulfate catalyst for decolorization of Rhodamine B in water. *RSC Advances*, *5*(41), 32520–32530. https://doi.org/10.1039/C5RA01447F

77 Tama, J., Riyani, K., & Setyaningtyas, T. (2020). Effect of ultraviolet and visible lights on degradation of congo red dye using $Fe^{2+}$/$H_2O_2$. *Journal of Physics: Conference Series*, *1494*(1), 012029. https://doi.org/10.1088/1742-6596/1494/1/012029

78 Said, M., Rizki, W. T., Asri, W. R., Desnelli, D., Rachmat, A., & Hariani, P. L. (2022). SnO2–Fe3O4 nanocomposites for the photodegradation of the Congo red dye. *Heliyon*, *8*(4), e09204. https://doi.org/10.1016/j.heliyon.2022.e09204

79 Shahid, M., Jingling, L., Ali, Z., Shakir, I., Warsi, M. F., Parveen, R., & Nadeem, M. (2013). Photocatalytic degradation of methylene blue on magnetically separable MgFe2O4 under visible light irradiation. *Materials Chemistry and Physics*, *139*(2–3), 566–571. https://doi.org/10.1016/j.matchemphys.2013.01.058